Journal of Advanced Ceramics
2023, **12**(4): 803–814
https://doi.org/10.26599/JAC.2023.9220721
ISSN 2226-4108
CN 10-1154/TQ

Research Article

The highest melting point material: Searched by Bayesian global optimization with deep potential molecular dynamics

Yinan Wang[a], Bo Wen[b], Xingjian Jiao[b], Ya Li[c], Lei Chen[d,e,*], Yujin Wang[d,e], Fu-Zhi Dai[a,f,*]

[a]*Artificial Intelligence for Science Institute, Beijing 100084, China*
[b]*Science and Technology on Advanced Functional Composite Laboratory, Aerospace Research Institute of Materials & Processing Technology, Beijing 100076, China*
[c]*College of Computer Science and Technology, Heilongjiang Institute of Technology, Harbin 150001, China*
[d]*Institute for Advanced Ceramics, School of Materials Science and Engineering, Harbin Institute of Technology, Harbin 150001, China*
[e]*Key Laboratory of Advanced Structural–Functional Integration Materials & Green Manufacturing Technology, Harbin Institute of Technology, Harbin 150001, China*
[f]*DP Technology, Beijing 100080, China*

Received: November 16, 2022; Revised: December 30, 2022; Accepted: January 19, 2023

Abstract: The interest in refractory materials is increasing rapidly in recent decades due to the development of hypersonic vehicles. However, the substance that has the highest melting point (T_m) keeps a secret, since precise measurements in extreme conditions are overwhelmingly difficult. In the present work, an accurate deep potential (DP) model of a Hf–Ta–C–N system was first trained, and then applied to search for the highest melting point material by molecular dynamics (MD) simulation and Bayesian global optimization (BGO). The predicted melting points agree well with the experiments and confirm that carbon site vacancies can enhance the melting point of rock-salt-structure carbides. The solid solution with N is verified as another new and more effective melting point enhancing approach for HfC, while a conventional routing of the solid solution with Ta (e.g., $HfTa_4C_5$) is not suggested to result in a maximum melting point. The highest melting point (~4236 K) is achieved with the composition of $HfC_{0.638}N_{0.271}$, which is ~80 K higher than the highest value in a Hf–C binary system. Dominating mechanism of the N addition is believed to be unstable C–N and N–N bonds in liquid phase, which reduces liquid phase entropy and renders the liquid phase less stable. The improved melting point and less gas generation during oxidation by the addition of N provide a new routing to modify thermal protection materials for the hypersonic vehicles.

Keywords: melting point (T_m); carbides; carbonitrides; deep potential (DP); Bayesian global optimization (BGO)

* Corresponding authors.
E-mail: L. Chen, chenleihit@hit.edu.cn;
F.-Z. Dai, dfzshiwo@163.com

1 Introduction

The interest in refractory materials is increasing rapidly in recent decades due to the development of the new generation of aerospace vehicles, where high-temperature (T) materials are widely applied in thermal protection systems, propulsion systems, etc. [1–9]. However, the substance that has the highest melting point (T_m) keeps a secret, the answer of which is of both scientific interest and technically demanding. It is well-known that tungsten has the highest melting point (~3700 K) among all the elements at the ambient pressure, which guarantees its widespread usage in high-temperature techniques. Another well-known refractory element is carbon, which sublimates instead of melting at the ambient pressure. It means that the melting point of carbon is not definable at the ambient pressure. Thus, there is no doubt about which element has the highest melting point. However, instead of the highest melting point element, we are concerned about which substance has the highest melting point. It is a controversial question for a long history, which has not reached an agreement until now.

People may blurt out the phrase "$HfTa_4C_5$ has the highest melting point of any known material: 4215 ℃", which has become ingrained in countless textbooks, and even in the 14th edition of Encyclopaedia Britannica [10–12]. However, the phrase results from a mistake due to unit conversion error, where the melting point of $HfTa_4C_5$ was reported to be "4215 in absolute temperature" in the original paper of Agte and Alterthum [11–13], which is 4215 K. A similar result that the solid solution between tantalum and hafnium carbides with Ta : Hf ≈ 4 : 1 exhibits the maximum melting point was reported by Andrievskii *et al*. [14], while Cedillos-Barraza *et al*. [15] only reported a local maximum melting point with Ta : Hf ≈ 4 : 1 and HfC having the highest melting point. Different from this viewpoint, there is another voice, which suggests that either tantalum or hafnium carbides has the highest melting point instead of their solid solution. In the 1960s, Rudy and Harmon [16–18] carried out systematic investigations on high- temperature materials, which were motivated by the development of the hypersonic vehicles. The phase diagrams and data from the project led by Rudy and Harmon [16–18] are still the most used by the researchers working on these materials. They reported that the highest melting points of tantalum and hafnium carbides appear at nonstoichiometric compositions. $TaC_{0.88}$ has the highest melting point of 4256±15 K in the tantalum carbides [16], while $HfC_{0.94}$ has the highest melting point of 4201±20 K in the hafnium carbides [17], which was later on corrected to 4223±20 K to account for zirconium impurities in the original hafnium used to prepare the carbides [18]. In addition, they revealed that melting point decreased monotonously from $TaC_{0.88}$ to $HfC_{0.94}$ without any local maximum in between. Even though the topic has been discussed for almost 100 years since the first report by Agte and Alterthum [13] in 1930, experimental measurements can hardly achieve agreement due to the following difficulties:

1) The real composition of a sample cannot be accurately controlled. On the one hand, there are many impurities in the sample, and the effects of the impurities on the melting point are unknown. On the other hand, carbon prefers to evaporate during heating, resulting in a different composition when reaching the melting point. As a result, the correlation between the melting point and the sample composition is not accurate.

2) Accurate temperature measurements at ultra-high temperatures are difficult. For example, corrections are necessary when converting the observed temperatures to true temperatures, or the true temperatures are derived based on the emissivity of materials, the exact values of which are not accurately known. Usually, the emissivity at other temperatures instead of that at the melting point is used, e.g., in the work by Cedillos-Barraza *et al*. [15] and by Savvatimskiy *et al*. [19]. Therefore, there are evident uncertainties in experimentally reported melting points.

Theoretical investigations are good complementary to experiments, which do not have the above limitations of experiments. Hong and van de Walle [20] adopted *ab initio* molecular dynamics (AIMD) to evaluate the melting points of tantalum and hafnium carbides and carbonitrides. They revealed that the calculated melting temperature dependence on the carbon content agrees with experiments, indicating the capability of theoretical approaches. Moreover, they reported that the addition of nitrogen may increase the melting temperature of hafnium carbides. However, due to the limited simulation size (no more than 64 atoms in the simulations by Hong and van de Walle [20]) and time in the AIMD, the composition and transition probability may not be adequately sampled. To overcome the shortcomings in the AIMD, we applied

deep potential molecular dynamics (DPMD) and Bayesian global optimization (BGO) to search for the highest melting point substance. In Section 2, the generation process and validation of a deep potential (DP) model are introduced. In Section 3, the dependence of the melting point on the composition in a rock-salt Hf–Ta–C–N system is determined, and the highest melting point composition is searched by the BGO.

2 Generation and validation of DP model

Even though it is still a controversy about what substance has the highest melting point, there is no doubt that the highest melting substance is among the tantalum and hafnium carbides or carbonitrides. Therefore, we focused on evaluating the composition-dependent melting point in the rock-salt-structure Hf–Ta–C–N system. To adequately sample the composition, we need molecular dynamics (MD) simulation methods with both high accuracy and high efficiency. Thanks to the developments in artificial intelligence, machine learning potentials [21–25] bridge the gap between density functional theory (DFT)-based methods and MD simulations, which combine high accuracy and low cost in atomistic simulations.

2. 1 Generation of DP model

The machine learning potential proposed by Zhang *et al*. [25,26], named DP, was adopted to train an interatomic potential for the Hf–Ta–C–N system from the dataset generated by DFT calculations. The dataset was explored by a concurrent learning scheme that is implemented in the DP-Generator (DP-GEN) software [27,28]. The DP-GEN software explores a configurational space, including both element distributions and conformation arrangements, iteratively in three steps: training, exploration, and labeling. During training, four different DP models with different activation functions and initialization parameters were trained based on the existing data. Then, hybrid MD and Monte Carlo (MC) simulations under isothermal–isobaric (NPT) ensemble were performed to sample configurational space. The explored thermodynamic states span the temperature range of 100–6000 K and the pressure range of −5–10 GPa. When $T > 3000$ K, only positive pressure was applied. Prediction accuracy of the configuration is measured by "model deviation", which is defined as the maximal standard deviation of forces predicted by the four DP models. Candidate configurations were randomly chosen from simulation trajectories if their model deviations were in a predefined range of ε_{low}–ε_{high}. The ε_{low}–ε_{high} was 0.3–0.5 when $T < 3000$ K and 0.5–1.0 when $T > 3000$ K. The selected configurations were then calculated by Vienna *ab initio* simulation package (VASP) [29,30]. Exchange-correlation energy was modeled by Perdew–Burke–Ernzerhof (PBE) functional [31]. The projector-augmented-wave (PAW) method [32,33] was used. Kinetic energy cut-off of a plane wave was set to be 900 eV. The *k*-point mesh according to the Monkhorst–Pack method [34] with a separation of 0.15 $Å^{-1}$ was adopted in Brillouin zone. Self-consistent field iteration stops when the difference in total energy of consecutive iterations is less than 10^{-6} eV. The DP-GEN iteration process was stopped when the prediction accuracy of the DP model was higher than 97% at each thermodynamic condition.

After collecting the dataset, the DP model was trained by the DeePMD-kit software [24]. The DP model maps local atomic configurations to atomic energy by deep neural networks [25,26], and has been proven to be applicable to many materials [35–41]. The DP model contains two sets of neural networks. The first one is a descriptor net, which automatically encodes the local atomic configurations to symmetry-preserving descriptors. The second one is a fitting net, which maps the symmetry-preserving descriptors to atomic energy. The architecture of the DP model is set as follows:

1) The smooth edition descriptor from Ref. [25] is used, which consists of three layers of neural networks with each layer having 25, 50, and 100 nodes. The projection dimension is set to 12. The cutoff is set to be 7.0 Å with a smooth function imposed from 2.0 Å. The "type-one" architecture is adopted to reduce the scale of the descriptor net. The activation functions are hyperbolic tangent (tanh).

2) The fitting net includes three layers of neural networks with each layer having 240, 240, and 240 nodes. A ResNet architecture is adopted in the fitting net. The activation functions are also tanh.

The model was trained in two rounds. Firstly, the model was trained from scratch. The learning rate decays from 1.0×10^{-3} to 1.0×10^{-8}, and the pre-factors of energy, force, and virial in a loss function change

from 0.01 to 1, from 100 to 1, and from 1 to 1, respectively. The DP model is initialized with some random seeds by the DeePMD-kit software. Then, the model was retrained with the model parameters inherited from the first training round. In this round, the learning rate decays from 1.0×10^{-4} to 1.0×10^{-8}, and the pre-factors of energy, force, and virial in the loss function are set to be 10, 1, and 1 without any change, respectively. In each training round, the total training step is 16 million. A batch size was determined automatically by the software based on the dataset, which was usually 1 or 2. For details of the parameters, please refer to Refs. [25,26] and the open-source software.

2. 2 Validation of DP model

The accuracy of the DP model was checked by comparing it with the DFT calculations. Figure 1(a) compares the energy predicted by the DP model with the DFT calculations, and Fig. 1(b) illustrates a distribution of a prediction error in the energy. Figure 1(c) compares the predicted force by the DP model with the DFT calculations, and Fig. 1(d) shows an error distribution of the prediction error in the force. The results reveal that the DP model agrees well with the DFT calculations, where the prediction errors in the energy and force are 8.1 meV/atom and 290 meV/Å, respectively. The prediction errors are comparable to those of many other similar systems, as reported in Refs. [38–40]. Table 1 compares the lattice parameter (a) and elastic constants (C_{11}, C_{12}, and C_{44}) of the rock-salt-structure HfC, TaC, HfN, and TaN predicted by the DP model with the DFT calculations, where excellent agreements can also be found. The bulk modulus (B), Young's modulus (E), and shear modulus (G) of polycrystalline HfC, TaC, HfN, and TaN are also estimated according to "Voigt–Reuss–Hill" approximation, and listed in Table 1. The equation of the state represents the variation of the energy with respect to a volume change, which is calculated by relaxing the structures at different volumes. Figure 2 compares the equations of the states of the rock-salt-structure HfC, HfN, TaC, and TaN predicted by the DP model with the DFT calculations, which all show good agreements. These comparisons reveal the accuracy of the DP model, which guarantees the trustable predictions in Section 3.

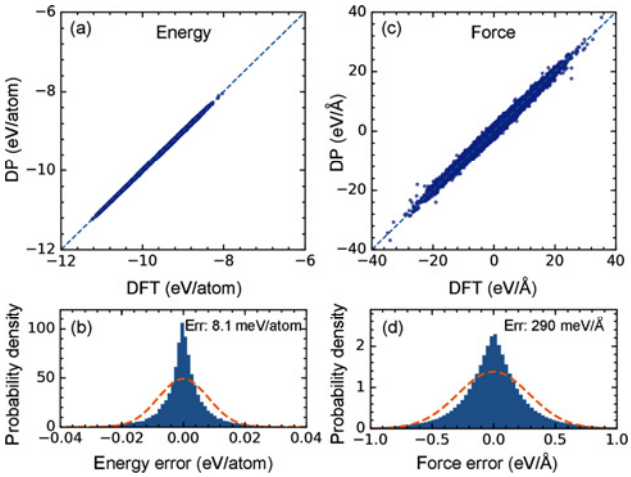

Fig. 1 Comparison of (a) energy and (c) force predicted by the DP model with DFT calculations and probability density distributions of prediction errors on (b) energy and (d) force.

Table 1 Comparison of DP prediction results with DFT calculations. DFT values were calculated with spacing of *k*-point mesh being 0.05 Å^{-1}. Δ is relative error between DP prediction and DFT calculations, which is $(v_{DP} - v_{DFT})/v_{DFT}$. v_{DP} means the value predicted by DP, while v_{DFT} means the value predicted by DFT

		a (Å)	Energy (eV/atom)	C_{11} (GPa)	C_{12} (GPa)	C_{44} (GPa)	B (GPa)	E (GPa)	G (GPa)
	DFT	4.647	−10.5253	513	105	172	241	440	184
HfC	DP	4.647	−10.5255	513	97	162	236	429	179
	Δ (%)	0.00	−0.002	0.0	−7.6	−5.8	−2.1	−2.5	−2.7
	DFT	4.479	−11.1039	708	134	176	325	527	214
TaC	DP	4.478	−11.1032	704	116	166	312	513	209
	Δ (%)	−0.02	0.006	−0.6	−13.4	−5.7	−4.0	−2.7	−2.3
	DFT	4.535	−10.8823	593	109	119	270	398	159
HfN	DP	4.536	−10.8824	587	116	113	273	385	152
	Δ (%)	0.02	−0.001	−1.0	6.4	−5.0	1.1	−3.3	−4.4
	DFT	4.421	−10.9177	718	137	60	331	321	120
TaN	DP	4.420	−10.9169	678	141	55	320	297	110
	Δ (%)	−0.02	0.007	−5.6	2.9	−8.3	−3.3	−7.5	−8.3

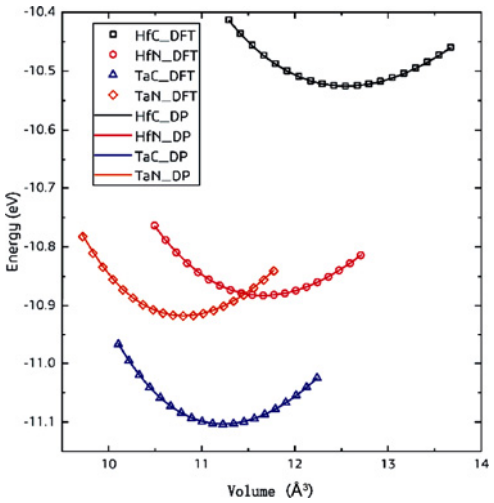

Fig. 2 Comparison of equations of states of rock-salt-structure HfC, HfN, TaC, and TaN predicted by the DP model with DFT calculations.

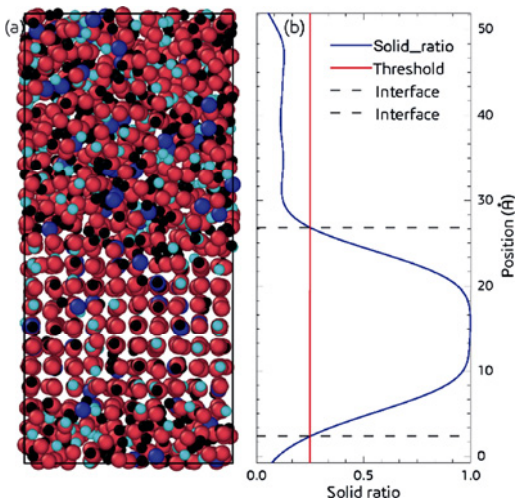

Fig 3 (a) Snapshot of solid–liquid coexistence configuration. Hf (big red atoms), Ta (big blue atoms), C (small black atoms), and N (small blue atoms) are distinguished by their sizes and colors. (b) Illustration of how interfaces between solid and liquid phases are detected by kernel density estimation and threshold value. The blue solid line is kernel density estimation of solid phase ratio along *Z* direction, while the vertical solid line is threshold value, and the horizontal dash lines indicate positions of interfaces.

3 Results and discussion

A solid–liquid coexistence MD simulation was adopted to evaluate the melting point of a given composition. The size of a simulation box was 5 × 5 × 10 ($X \times Y \times Z$) unitcells, and the interfaces between the solid and liquid phases were along the *Z* direction. The timestep in the MD simulations was set to be 1 fs. The NPT ensemble was adopted during the simulations. The system was firstly equilibrated at 3500 K for 50 ps, and half of the system was heated to 5000 K to melt and equilibrated for 50 ps with the other half frozen. Then, the whole system was set to different temperatures and equilibrated for 100 ps to search for the melting point. Figure 3(a) illustrates a snapshot of the solid–liquid coexistence configuration after equilibrium. In principle, when simulating at the melting point, existence probabilities of the solid and liquid phases are the same, which means that their amounts are the same in the coexistence configuration. Figure 3(b) illustrates how the interfaces between the solid and liquid phases are detected by kernel density estimation (the density of the solid phase along the *Z* direction) and a threshold value. Thus, a solid-to-liquid ratio can be detected. A series of temperatures with a step of 5 K were simulated. Then, the variation of the solid ratio with respect to the temperature was fitted, and the melting point was predicted to be the temperature with a solid ratio of 0.5. During the fitting, the configurations with a solid ratio higher than 0.95 or lower than 0.05 were excluded. The MD simulations were implemented with LAMMPS software [42,43] compiled with DeePMD-kit package.

3.1 Melting points in HfC_{1-x} and TaC_{1-x}

In HfC or TaC, it has reached a consensus that the highest melting point appears at a nonstoichiometric composition with the depletion of C. Here, we checked the reliability of the DP model in predicting this phenomenon and the accuracy in predicting the melting points. The melting points of a series of HfC_{1-x} and TaC_{1-x} are calculated, where x changes from 0 to 0.2 with a step of 0.02. The predicted results are shown in Fig. 4, together with the experimental measurements by Rudy and Harmon [16–18] in the 1960s and by Sheindlin *et al*. [44] in recent years and the results calculated by Hong and van de Walle [20] using the AIMD for comparison. In the experiments, there are two melting point values related to a given composition, which are indicated as solid and liquid lines in a phase diagram, as shown in Fig. 4. The solid line is the temperature when the solid phase starts to melt, while the liquid line is the temperature when the liquid phase starts to freeze. The compositions of the solid and liquid phases in equilibrium are usually different from each other. This phenomenon cannot be

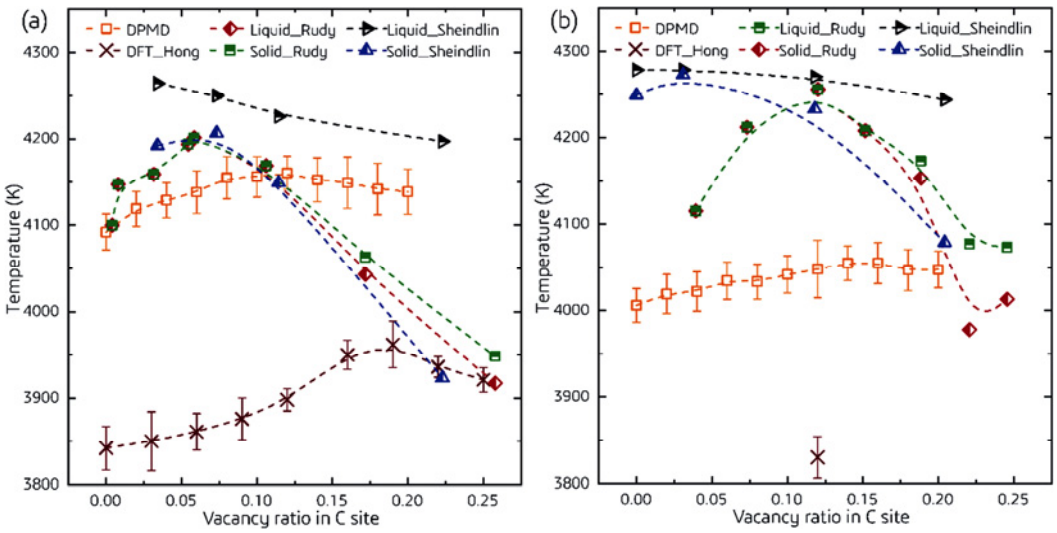

Fig. 4 Comparison of calculated and measured melting points of (a) HfC_{1-x} and (b) TaC_{1-x}. DPMD represents the results calculated in this work. DFT_Hong means the results calculated by Hong and van de Walle [20] using DFT. Liquid_Rudy and Solid_Rudy, and Liquid_Sheindlin and Solid_Sheindlin are the experimental liquid and solid lines of phase diagrams measured by Rudy and Harmon [16–18] and Sheindlin *et al*. [44], respectively.

captured by our simulation, since the compositions of the solid and liquid phases are the same in the simulations. Nevertheless, it is clear that the predicted results by the DP model agree with the experiments, which confirm that the nonstoichiometric composition with the depletion of C has the highest melting point in both HfC_{1-x} and TaC_{1-x}. For HfC_{1-x}, the maximum melting point is reached at $x \approx 0.12$. For TaC_{1-x}, the highest melting point composition is $x \approx 0.14$. The highest melting point compositions in the experiments are $x \approx 0.06$ for HfC_{1-x} and $x \approx 0.12$ for TaC_{1-x} by Rudy and Harmon [16–18], and $x \approx 0.07$ for HfC_{1-x} and $x \approx 0.03$ for TaC_{1-x} by Sheindlin *et al*. [44]. The predicted highest melting point of HfC_{1-x} is ~4160 K, ~60 K lower than the experimental results reported by Rudy and Harmon [16–18], while the predicted highest melting point of TaC_{1-x} is ~4050 K, ~200 K lower than the experimental results reported by Rudy and Harmon [16–18]. In comparison to the results calculated by Hong and van de Walle [20] using the AIMD, our calculated melting points are ~200 K higher, which agree much better with the experiments. In addition, the highest melting compositions predicted by the DPMD match better with the experiments by Rudy and Harmon [16–18] in comparison to the compositions predicted by the AIMD by Hong and van de Walle [20]. For example, the highest composition in HfC_{1-x} is $x \approx 0.19$ in the AIMD by Hong and van de Walle [20], as shown in Fig. 4(a). The better agreements of our simulations may result from the more adequate sampling with bigger simulation systems and longer simulation time.

3.2 Melting points in $Hf_{1-y}Ta_yC_{0.88}$

It has long been a controversy that whether there is a global maximum melting point in the solid solution between HfC_{1-x} and TaC_{1-x}. To clarify this controversy, the melting points of a series of $Hf_{1-y}Ta_yC_{0.88}$ are calculated, where y changes from 0.0 to 1.0 with a step of 0.1. As shown in Fig. 4, both HfC_{1-x} and TaC_{1-x} roughly have their highest melting point with $x \approx 0.12$. Therefore, the vacancy concentration in the C site was set to 0.12. The predicted results are shown in Fig. 5, together with the experimental results by Agte and Alterthum [13], Andrievskii *et al*. [14], Rudy and Harmon [16–18], and Cedillos-Barraza *et al*. [15] and the results calculated by Hong and van de Walle [20] using the AIMD for comparison. Our results reveal that the melting point changes monotonously between $HfC_{0.88}$ and $TaC_{0.88}$ without any local maximum or minimum in between. However, the variation of the melting point with respect to the Ta content predicted by Hong and van de Walle [20] is rugged, which may result from inadequate sampling by the AIMD. Thus, it can hardly say whether there is a local or global maximum or minimum in between or not. Our simulation results agree with the results reported by Rudy and Harmon [16–18] and by Cedillos-Barraza *et al*. [15], which do not support the conclusion that $HfTa_4C_5$ exhibits the highest melting point, even though

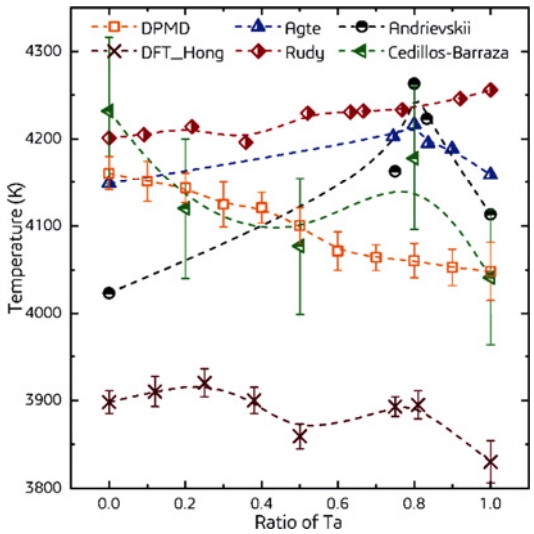

Fig. 5 Comparison of calculated and measured melting points of $Hf_{1-y}Ta_yC_{1-x}$. DPMD represents results of $Hf_{1-y}Ta_yC_{0.88}$ calculated in this work. DFT_Hong means the results calculated by Hong and van de Walle [20] using DFT. Agte, Rudy, Andrievskii, and Cedillos-Barraza are the experimental results by Agte and Alterthum [13], Rudy and Harmon [16–18], Andrievskii *et al*. [14], and Cedillos-Barraza *et al*. [15], respectively.

the results by Agte and Alterthum [13] and Andrievskii *et al*. [14] argued that the global maximum melting point existed in the HfC_{1-x} and TaC_{1-x} solid solution ($HfTa_4C_5$). In the calculations, according to both our results and the results reported by Hong and van de Walle [20], the melting points of HfC_{1-x} are ~100 K higher than those of TaC_{1-x}. In the experiments, it has been reported that either TaC_{1-x} or HfC_{1-x} had a slightly higher melting point. For example, Rudy and Harmon [16–18] reported that the melting points of TaC_{1-x} were slightly higher, while Cedillos-Barraza *et al*. [15] reported that the melting points of HfC_{1-x} were slightly higher. Due to the errors in the DFT calculations, DP model, and experimental measurements (the errors will be discussed in Section 3.4), it can hardly say whether the melting point of HfC_{1-x} or TaC_{1-x} is higher, since conflict results were reported by different researchers.

3. 3 Searching for the highest melting point by BGO

Hong and van de Walle [20] have reported that the addition of N may increase the melting point of HfC_{1-x}. To search for the possible highest melting point composition, we calculated the melting points of $Hf_{1-y}Ta_yC_{1-x-z}N_z$ with y = 0–1, x = 0–0.3, and z = 0–0.5, where x is the vacancy concentration in the C site. The smallest steps in x, y, and z are all 1/500 according to the simulation cell size, resulting in a quite large searching space with 10^6 in magnitude. The BGO was adopted to improve the searching efficiency, the process of which is illustrated in Fig. 6(a). The software package "BayesianOptimization" [45] was adopted to implement the BGO. The BGO searches for the highest melting point in an iterative way, which allows us to effectively navigate the search space iteratively to identify promising candidates for guiding simulations [46]. The approach relies on the use of uncertainties and making predictions from a surrogate model together with a utility function that prioritizes a decision-making process on unexplored data [46]. People who are interested in the approach and how to apply the method in practice can refer to Refs. [45,46]. By the BGO, the surrogate model that fits the dependence of the melting point (T_m) on the composition ((x, y, z)) based on the existing data is trained first. Then, a new data point is calculated based on the guidance of the surrogate model and utility function. A Gaussian process was adopted as the surrogate model here. The upper confidence bound with κ = 2.5 was adopted as the utility function, which means that the next composition to try is the one that has the highest $\mu + \kappa\sigma$, where μ and σ are the mean and standard errors predicted by the Gaussian process model, respectively, and k is the hyper-parameter. With the iterative addition of new data points and improvements on the surrogate model, the highest melting point will be found efficiently. The search was stopped when no higher melting point composition can be found in 50 iterations.

The variation of the highest melting point in the dataset with respect to the iteration step is shown in Fig. 6(b). It reveals that the BGO can search for the highest melting point in an efficient way, where the highest melting point increases by ~60 K within 30 steps. The obtained highest melting point is 4236 K with its corresponding composition being x = 0.091, y = 0.000, and z = 0.271 (the chemical formula is $HfC_{0.638}N_{0.271}$), which is ~80 K higher than the melting point of $HfC_{0.88}$. Figure 6(c) shows the relationship between T_m and (x, y, z). The data of Fig. 6(c) are listed in Table S1 in the Electronic Supplementary Material (ESM). The bigger the point is, the higher the melting point is. In agreement with results reported by Hong and van de Walle [20], the addition of N can efficiently increase the melting point of HfC_{1-x}, even though the melting points of HfN (~3705 K by the DPMD and ~3663 K in the experiments) are much lower than that of

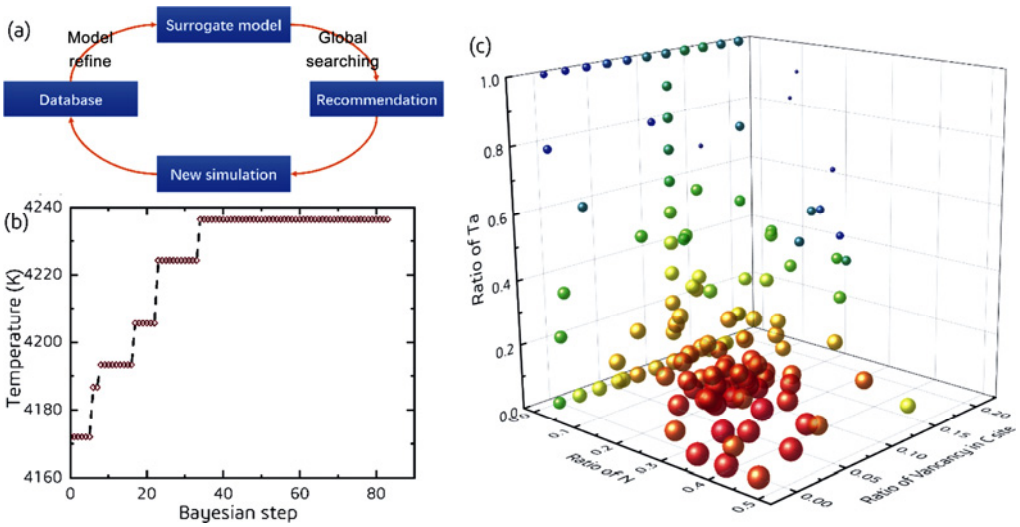

Fig. 6 (a) Schematic illustration of BGO. (b) Variation of searched highest melting point as a function of iteration step. (c) Variation of melting point with respect to composition of $Hf_{1-y}Ta_yC_{1-x-z}N_z$. In (c), the bigger the sphere is, the higher the melting point is. The smallest melting point and the highest melting point in (c) are 3908 and 4236 K, respectively.

HfC. The addition of N plays a similar tendency to the C-site vacancy on the melting point of HfC, where the melting point first increases, and then decreases with the addition of N, resulting in the maximum value. The increasing effect on the melting point due to the N addition (increased by ~120 K at most in comparison to that of HfC) is more significant than that on introducing the C-site vacancy (increased by ~60 K at most in comparison to that of HfC). The incorporation of both N addition and C-site vacancy results in the highest melting point. Different from that of HfC, the addition of N will reduce the melting point of TaC. As can be seen from Fig. 6(c), TaC_{1-x} is not the composition with the lowest melting point, which indicates that the addition of N will reduce the melting point of TaC. The effects of the N addition on the melting point of HfC and TaC are shown in Fig. S2 in the ESM. The reason for the decreased melting point may be that the rock-salt TaN is not in a stable phase. Thus, the addition of N in TaC reduces the stability of the solid phase.

3. 4 Discussion

It is well-known that a higher melting point can be achieved by the nonstoichiometric composition with the depletion of C in HfC and TaC, which is also confirmed by our simulations. However, the long-time controversy that whether there is the highest melting point solid solution between HfC and TaC still needs further investigation. Our simulations do not support this assumption and suggest a monotonous change of the melting point between HfC and TaC, which agrees with the experimental results of Rudy and Harmon [16–18]. Except for the C-site vacancy, we verified another intriguing melting point enhancing mechanism discovered by Hong and van de Walle [20]. Substituting C by N is more effective in improving the melting point of HfC in comparison to the C-site vacancy. As suggested by Hong and van de Walle [20], the addition of N remarkably changes a liquid structure due to the instability of the C–N and N–N bonds. Liquid is stabilized by its higher entropy to offset its higher enthalpy. In particular, the higher entropy of liquid is reflected by its large variety of pair-wise correlations. For example, the exceeding entropy of liquid with respect to ideal gas is dominated by the two-body exceeding entropy (S_{ex}/k_B), which is

$$S_{ex}/k_B = -2\pi\rho\sum_{i,j}x_i x_j\int_0^\infty [g_{ij}(r)\ln g_{ij}(r)-(g_{ij}(r)-1)]\,r^2\mathrm{d}r \quad (1)$$

where ρ is the atomic number density, x_i and x_j are the fractional compositions, g_{ij} is the pair correlation function between the elements i and j, and r is the distance from the atom j to the atom i. Figure 7 shows the pair correlation function of HfC, HfN, and $HfC_{0.5}N_{0.5}$ liquid obtained at 4500 K and their S_{ex}/k_B. It is evident that the dominant first neighbor of N is Hf, indicating low stability of the C–N and N–N bonds in the liquid phase. In contrast, the C–C bond is stable, forming a strong first neighbor correlation peak, where even C chains with more than three C atoms are found in the

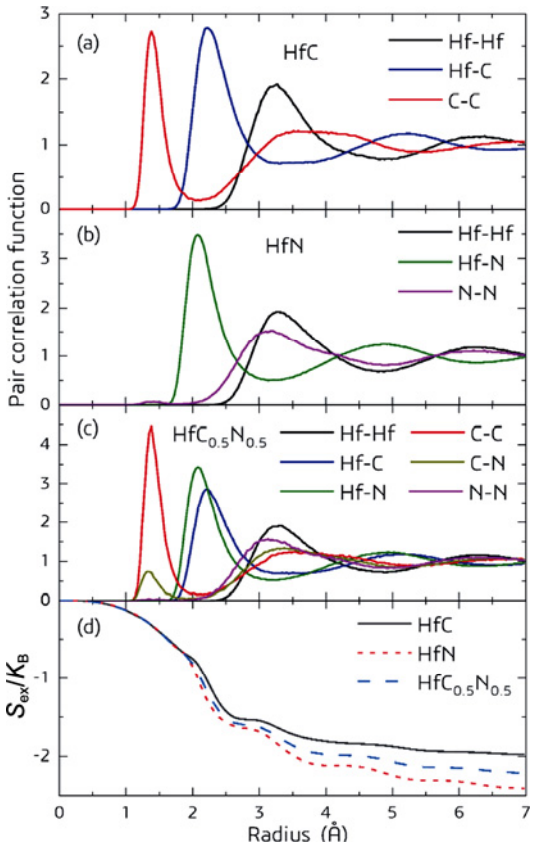

Fig. 7 Pair correlation function (normalized as $r \to +\infty$) in liquid-state (a) HfC, (b) HfN, and (c) $HfC_{0.5}N_{0.5}$. (d) Comparison of S_{ex}/k_B of liquid-state HfC, HfN, and $HfC_{0.5}N_{0.5}$.

simulated atomic structure. The reduced variety of pair-wise correlations with the addition of N leads to lower entropy of the liquid phase (Fig. 7(d)), and renders the liquid phase less stable. Moreover, the solid solution of N will increase the solid-state configurational entropy and renders the solid phase more stable. As a result, the addition of N enhances the melting point of HfC.

Even though almost 100 years have passed since the first report by Agte and Alterthum [13] in 1930, it is still non-trial to answer the question "which substance has the highest melting point at the ambient pressure?", since there are large errors in both experiments and simulations. Therefore, there are significant discrepancies between the results reported by different researchers, either experimental results or simulation results. In the experiments, the composition of the materials cannot be exactly controlled or determined due to the difficulties in the sample preparation, the sample interaction with a crucible, and the sample evaporation during heating; the determination of the real temperature is also problematic due to extreme conditions, equipment instability, etc. For example, Andrievskii *et al*. [14] reported that some of their samples contained high contents of N and O, around 10% that of C, Cedillos-Barraza *et al*. [15] also reported similar high impurities in their HfC sample, and Savvatimskiy *et al*. [47] detected a high content of O in their sample. These impurities may lead to substantial shifts in the melting points, and the relation between the composition and the melting point is not reliable. In the early years, the samples were heated by Joule heating, a slow heating effect of which would lead to the preferred evaporation of C, resulting in a different composition when approaching the melting point. Laser heating technology developed in recent years can be conducted under containerless conditions [15,19,44,47], which overcomes the problem of the composition shift during heating. However, a narrow time window further challenges the temperature measurement. Cedillos-Barraza *et al*. [15] and Savvatimskiy *et al*. [19] used different emissivity to estimate the temperature, and suggested fully different conclusions on whether $HfTa_4C_5$ had the highest melting point. In addition, the flash melting by laser heating may lead to results that deviate from equilibrium. Therefore, using the data to reproduce the phase diagram is questionable. In the simulations, there are also many errors, e.g., insufficient energy cutoff and *k*-spacing, intrinsic error due to exchange-correlation functionals, fitting errors of interatomic potentials, and inadequate sampling in the simulations. Hong and van de Walle [20] estimated in their work that the simulated melting points may shift upwards by ~460 K when using the more accurate Heyd–Scuseria–Ernzerhof (HSE) hybrid functional to replace the PBE functional. The melting points in our simulations shifted upwards by ~200 K in comparison to the results calculated by Hong and van de Walle [20], which may result from different simulation approaches and different accuracy of calculation methods. To obtain more reliable predictions, the interatomic potentials fitted to more accurate quantum mechanical data, e.g., using HSE hybrid functional, are needed. In addition, more accurate simulation methods that can obtain the thermodynamic equilibrium between the solid and liquid phases are also necessary, e.g., determining a chemical potential of each element by the simulations. Then, the solid and liquid lines in the experiments may be reproduced by the simulations. Nevertheless, our simulation results can still provide the valuable information on understanding the dependence

of the melting points on the compositions and searching for high melting point materials for the applications in extreme conditions, e.g., thermal protection systems in the hypersonic vehicles. HfC is one of the promising compounds applied in the thermal protection systems of the hypersonic vehicles due to its high melting point and the high melting point of its oxidation product, HfO_2. The addition of N, on the one hand, will improve the melting point of HfC, and on the other hand, will reduce the amount of gas generated during the oxidation, resulting in better oxidation scales, and may render a better thermal protection effect.

4 Conclusions

In the present work, the highest melting point challenge was investigated by MD simulations based on an accurate DP model of a Hf–Ta–C–N system. The predicted melting points are consistent with the experimental measurements, indicating the reliability of the simulations. Our results confirmed the well-known phenomenon that the C-site vacancy is a melting point-enhancing mechanism in rock-salt-structure transition metal carbides. The long-time controversy that whether the solid solution $HfTa_4C_5$ is the highest melting point substance keeps unsolved. Our simulations do not support this assumption, and more precise methods are needed to clarify this assumption in the future. In HfC, the addition of N is verified as another melting point-enhancing approach, which is more effective than that of the C-site vacancy. The addition of N remarkably reduces the pair correlation of C–N and N–N, reduces the entropy of the liquid phase, and renders the liquid phase less stable. The enhanced melting point and less gas generation during the oxidation by the addition of N provide a new routing to modify the thermal protection materials for the hypersonic vehicles.

Acknowledgements

Dr. Lei Chen would thank for the supports by the National Natural Science Foundation of China (Nos. 52032002, 51972081, and U2130103), University Nursing Program for Young Scholars with Creative Talents in Heilongjiang Province (No. UNPYSCT-2020052), and Heilongjiang Touyan Team Program. This work was supported by Bohrium Cloud Platform of DP Technology.

Electronic Supplementary Material

Supplementary material is available in the online version of this article at https://doi.org/10.26599/JAC.2023.9220721.

References

[1] Fahrenholtz WG, Hilmas GE, Talmy IG, *et al*. Refractory diborides of zirconium and hafnium. *J Am Ceram Soc* 2007, **90**: 1347–1364.

[2] Katoh Y, Vasudevamurthy G, Nozawa T, *et al*. Properties of zirconium carbide for nuclear fuel applications. *J Nucl Mater* 2013, **441**: 718–742.

[3] Opeka MM, Talmy IG, Zaykoski JA. Oxidation-based materials selection for 2000 ℃+ hypersonic aerosurfaces: Theoretical considerations and historical experience. *J Mater Sci* 2004, **39**: 5887–5904.

[4] Binner J, Porter M, Baker B, *et al*. Selection, processing, properties and applications of ultra-high temperature ceramic matrix composites, UHTCMCs—A review. *Int Mater Rev* 2020, **65**: 389–444.

[5] Ni DW, Cheng Y, Zhang JP, *et al*. Advances in ultra-high temperature ceramics, composites, and coatings. *J Adv Ceram* 2022, **11**: 1–56.

[6] Ye ZM, Zeng Y, Xiong X, *et al*. Elucidating the role of preferential oxidation during ablation: Insights on the design and optimization of multicomponent ultra-high temperature ceramics. *J Adv Ceram* 2022, **11**: 1956–1975.

[7] Xiang HM, Xing Y, Dai FZ, *et al*. High-entropy ceramics: Present status, challenges, and a look forward. *J Adv Ceram* 2021, **10**: 385–441.

[8] Liu SY, Zhang SX, Liu SY, *et al*. Phase stability, mechanical properties and melting points of high-entropy quaternary metal carbides from first-principles. *J Eur Ceram Soc* 2021, **41**: 6267–6274.

[9] Liu SY, Zhang SX, Liu SY, *et al*. Stability and mechanical properties of single-phase quinary high-entropy metal carbides: First-principles theory and thermodynamics. *J Eur Ceram Soc* 2022, **42**: 3089–3098.

[10] Emsley J. *Nature's Building Blocks*, 2nd edn. Oxford, UK: Oxford University Press, 2011.

[11] Arblaster J. The highest melting point challenge. *Anal Bioanal Chem* 2015, **407**: 3265.

[12] Arblaster J. Solution to highest melting point challenge. *Anal Bioanal Chem* 2015, **407**: 6589–6590.

[13] Agte C, Alterthum H. Systems of high-melting carbides: Contributions to the problem of carbon fusion. *Z Tech Phys* 1930, **11**: 182–191. (in German)

[14] Andrievskii RA, Strel'nikova NS, Poltoratskii NI, *et al*. Melting point in systems ZrC–HfC, TaC–ZrC, TaC–HfC. *Powder Metall Met C*+ 1967, **6**: 65–67.

[15] Cedillos-Barraza O, Manara D, Boboridis K, *et al*. Investigating the highest melting temperature materials: A

laser melting study of the TaC–HfC system. *Sci Rep* 2016, **6**: 37962.

[16] Rudy E, Harmon DP. Ternary phase equilibria in transition metal–boron–carbon–silicon systems. Part 1. Related binary systems. Vol. 5. Ta–C system. Partial investigation in the systems Nb–C and VC. In: *Technical Report from Aerojet-General Corp.*, Sacramento, USA, 1965.

[17] Rudy E. Ternary phase equilibria in transition metal–boron–carbon–silicon systems. Part 1. Related binary systems. Vol. 4. Hf–C system. In: *Technical Report from Aerojet-General Corp.*, Sacramento, USA, 1965.

[18] Rudy E. Ternary phase equilibria in transition metal–boron–carbon–silicon systems. Part 2. Ternary systems. Vol. 1. Ta–Hf–C system. In: *Technical Report from Aerojet-General Corp.*, Sacramento, USA, 1965.

[19] Savvatimskiy AI, Onufriev SV, Muboyadzhyan SA. Thermophysical properties of the most refractory carbide $Ta_{0.8}Hf_{0.2}C$ under high temperatures (2000–5000 K). *J Eur Ceram Soc* 2019, **39**: 907–914.

[20] Hong QJ, van de Walle A. Prediction of the material with highest known melting point from *ab initio* molecular dynamics calculations. *Phys Rev B* 2015, **92**: 020104.

[21] Behler J, Parrinello M. Generalized neural-network representation of high-dimensional potential-energy surfaces. *Phys Rev Lett* 2007, **98**: 146401.

[22] Bartók AP, Payne MC, Kondor R, *et al*. Gaussian approximation potentials: The accuracy of quantum mechanics, without the electrons. *Phys Rev Lett* 2010, **104**: 136403.

[23] Thompson AP, Swiler LP, Trott CR, *et al*. Spectral neighbor analysis method for automated generation of quantum-accurate interatomic potentials. *J Comput Phys* 2015, **285**: 316–330.

[24] Schütt KT, Arbabzadah F, Chmiela S, *et al*. Quantum-chemical insights from deep tensor neural networks. *Nat Commun* 2017, **8**: 13890.

[25] Zhang LF, Han JQ, Wang H, *et al*. Deep potential molecular dynamics: A scalable model with the accuracy of quantum mechanics. *Phys Rev Lett* 2018, **120**: 143001.

[26] Wang H, Zhang LF, Han JQ, *et al*. DeePMD-kit: A deep learning package for many-body potential energy representation and molecular dynamics. *Comput Phys Commun* 2018, **228**: 178–184.

[27] Zhang LF, Lin DY, Wang H, *et al*. Active learning of uniformly accurate interatomic potentials for materials simulation. *Phys Rev Mater* 2019, **3**: 023804.

[28] Zhang YZ, Wang HD, Chen WJ, *et al*. DP-GEN: A concurrent learning platform for the generation of reliable deep learning based potential energy models. *Comput Phys Commun* 2020, **253**: 107206.

[29] Kresse G, Furthmüller J. Efficient iterative schemes for *ab initio* total-energy calculations using a plane-wave basis set. *Phys Rev B* 1996, **54**: 11169–11186.

[30] Kresse G, Furthmüller J. Efficiency of *ab-initio* total energy calculations for metals and semiconductors using a plane-wave basis set. *Comput Mater Sci* 1996, **6**: 15–50.

[31] Perdew JP, Burke K, Ernzerhof M. Generalized gradient approximation made simple. *Phys Rev Lett* 1996, **77**: 3865–3868.

[32] Blöchl PE. Projector augmented-wave method. *Phys Rev B* 1994, **50**: 17953–17979.

[33] Kresse G, Joubert D. From ultrasoft pseudopotentials to the projector augmented-wave method. *Phys Rev B* 1999, **59**: 1758–1775.

[34] Monkhorst HJ, Pack JD. Special points for Brillouin-zone integrations. *Phys Rev B* 1976, **13**: 5188–5192.

[35] Jiang WR, Zhang YZ, Zhang LF, *et al*. Accurate Deep Potential model for the Al–Cu–Mg alloy in the full concentration space. *Chin Phys B* 2021, **30**: 050706.

[36] Wang YN, Zhang LF, Xu B, *et al*. A generalizable machine learning potential of Ag–Au nanoalloys and its application to surface reconstruction, segregation and diffusion. *Model Simul Mater Sc* 2022, **30**: 025003.

[37] Wen TQ, Wang R, Zhu LY, *et al*. Specialising neural network potentials for accurate properties and application to the mechanical response of titanium. *npj Comput Mater* 2021, **7**: 206.

[38] Dai FZ, Wen B, Sun YJ, *et al*. Theoretical prediction on thermal and mechanical properties of high entropy $(Zr_{0.2}Hf_{0.2}Ti_{0.2}Nb_{0.2}Ta_{0.2})C$ by deep learning potential. *J Mater Sci Technol* 2020, **43**: 168–174.

[39] Dai FZ, Sun YJ, Wen B, *et al*. Temperature dependent thermal and elastic properties of high entropy $(Ti_{0.2}Zr_{0.2}Hf_{0.2}Nb_{0.2}Ta_{0.2})B_2$: Molecular dynamics simulation by deep learning potential. *J Mater Sci Technol* 2021, **72**: 8–15.

[40] Dai FZ, Wen B, Sun YJ, *et al*. Grain boundary segregation induced strong UHTCs at elevated temperatures: A universal mechanism from conventional UHTCs to high entropy UHTCs. *J Mater Sci Technol* 2022, **123**: 26–33.

[41] Wang XY, Wang YN, Zhang LF, *et al*. A tungsten deep neural-network potential for simulating mechanical property degradation under fusion service environment. *Nucl Fusion* 2022, **62**: 126013.

[42] Plimpton S. Fast parallel algorithms for short-range molecular dynamics. *J Comput Phys* 1995, **117**: 1–19.

[43] Thompson AP, Aktulga HM, Berger R, *et al*. LAMMPS—A flexible simulation tool for particle-based materials modeling at the atomic, meso, and continuum scales. *Comput Phys Commun* 2022, **271**: 108171.

[44] Sheindlin M, Falyakhov T, Petukhov S, *et al*. Recent advances in the study of high-temperature behaviour of non-stoichiometric TaC_x, HfC_x and ZrC_x carbides in the domain of their congruent melting point. *Adv Appl Ceram* 2018, **117**: s48–s55.

[45] Nogueira F. Bayesian optimization: Open source constrained global optimization tool for Python. Information on https://github.com/fmfn/BayesianOptimization, 2014.

[46] Lookman T, Balachandran PV, Xue DZ, *et al*. Active learning in materials science with emphasis on adaptive sampling using uncertainties for targeted design. *npj Comput Mater* 2019, **5**: 21.

[47] Savvatimskiy AI, Onufriev SV, Valyano GE, *et al*. Thermophysical properties for hafnium carbide (HfC) versus temperature from 2000 to 5000 K (experiment). *J Mater Sci* 2020, **55**: 13559–13568.